PHYSICAL REVIEW B **93**, 134303 (2016)

Ferroelectricity in corundum derivatives

Meng Ye* and David Vanderbilt
Department of Physics & Astronomy, Rutgers University, Piscataway, New Jersey 08854, USA
(Received 11 February 2016; published 4 April 2016)

The search for new ferroelectric (FE) materials holds promise for broadening our understanding of FE mechanisms and extending the range of application of FE materials. Here we investigate a class of ABO_3 and $A_2BB'O_6$ materials that can be derived from the X_2O_3 corundum structure by mixing two or three ordered cations on the X site. Most such corundum derivatives have a polar structure, but it is unclear whether the polarization is reversible, which is a requirement for a FE material. In this paper, we propose a method to study the FE reversal path of materials in the corundum derivative family. We first categorize the corundum derivatives into four classes and show that only two of these allow for the possibility of FE reversal. We then calculate the energy profile and energy barrier of the FE reversal path using first-principles density functional methods with a structural constraint. Furthermore, we identify several empirical measures that can provide a rule of thumb for estimating the energy barriers. Finally, the conditions under which the magnetic ordering is compatible with ferroelectricity are determined. These results lead us to predict several potentially new FE materials.

DOI: 10.1103/PhysRevB.93.134303

I. INTRODUCTION

Ferroelectricity requires a material to have a spontaneous electric polarization that can be reversed by an external electric field [1]. The search for new ferroelectric (FE) materials holds promise for broadening our understanding of FE mechanisms and extending the range of application of FE materials. A switchable spontaneous polarization implies a hysteresis effect that can be used in memory devices [2]. FE materials also exhibit high and tunable electric permittivity, which can be used in capacitors to increase the capacitance and reduce the size of devices. In addition, FE materials are piezoelectric and pyroelectric, according to symmetry considerations. These combined properties make FE materials ideal for electric, mechanical, and thermal sensors. Recently, research on multiferroics, in which FE and ferromagnetic orders coexist in the same material, has further extended the range of application of FE materials [3–9].

The most intensively studied family of FE oxides is that of the perovskite oxides such as $BaTiO_3$[10,11]. Perovskite oxides have the chemical formula ABO_3 with the A cation much larger than the B cation. The FE distortion is usually driven by B-site off-centering and typically requires an empty d shell on the B cation, which is not compatible with magnetism. Recently, rocksalt-ordered $A_2BB'O_6$ double perovskites (and more complex $AA'BB'O_6$ materials) have also attracted great interest [12,13].

The corundum derivatives ABO_3 and $A_2BB'O_6$ make up a family of oxides that can be derived from the corundum structure with cation ordering. Most corundum derivatives are polar and thus can potentially be new FE oxides [17–32]. $LiNbO_3$ (LNO) is a well-known example of a FE corundum derivative [14–16]. Despite the similar chemical formula, corundum derivatives are different from perovskites in many aspects. The high-symmetry parent structure is rhombohedral for corundum derivatives but cubic for perovskites. The polarization reversal mechanisms are also distinct. In corundum derivatives, the polarization reversal is driven by the small A or B cations migrating between oxygen octahedra [15,16], so that d^0 configuration is not required. This is in contrast to the off-centering displacement of d^0B cations in the oxygen octahedra in most perovskites. The huge number of potential combinations of A, B, and B' cations in the corundum-derivative family opens the possibility to achieve not only ferroelectricity but also multiferroicity [18,19].

In this paper, we use first-principles density functional methods to systematically study the polar structure and the coherent FE reversal paths for a variety of corundum derivatives. First, the structures of corundum derivatives are introduced in Sec. II A. Then the structural criteria for corundum derivatives to be FE are discussed in Sec. II B. In Sec. II C, we propose a systematic method to analyze the coherent FE barrier and energy profile. Lastly, the new method is applied to several corundum derivatives, and empirical measures that can provide a rule of thumb for estimating the reversal barrier are summarized in Sec. III.

II. PRELIMINARY

A. Structure

The corundum derivatives ABO_3 and $A_2BB'O_6$ can be derived from the corundum structure X_2O_3 with cation ordering as shown in Fig. 1. In the 10-atom rhombohedral unit cell, the cations are spaced along the threefold rotation axis and each one is surrounded by a distorted oxygen octahedron. Two thirds of the oxygen octahedra are filled with cations, while one third of them are cation vacant.

Based on the combinations and arrangements of cations, the corundum derivatives can be classified into four types, which we denote as follows. An oxygen octahedron with an A or B cation inside is written as "A" or "B," and if an oxygen octahedron is cation-vacant, the octahedron is denoted by "$-$." This notation is then used to represent the column of six face-sharing oxygen octahedra in the unit cell for each of the four different types of corundum derivatives. Thus, the LNO-type ABO_3 is $AB-AB-$, the ilmenite ABO_3 is $AB-BA-$,

*mengye@physics.rutgers.edu

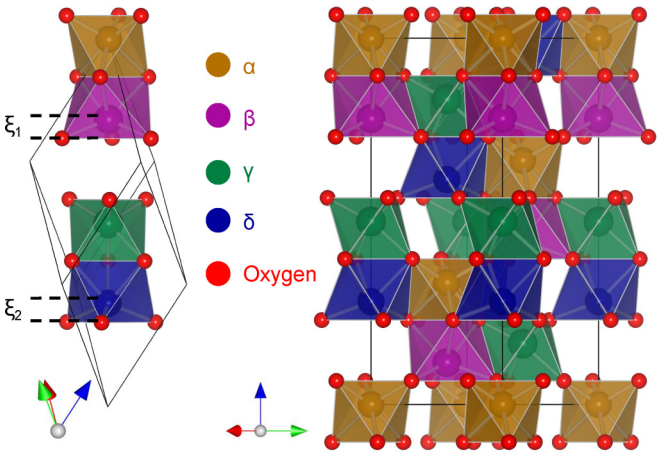

FIG. 1. Structure of corundum derivatives. The unit cell in the rhombohedral setting is shown at the left; an enlarged hexagonal-setting view is shown at right. The cations α, β, γ, and δ are all identical in the X_2O_3 corundum structure. For the LNO-type ABO_3, $\beta = \delta = A$, $\alpha = \gamma = B$; for the ilmenite ABO_3, $\beta = \gamma = A$, $\alpha = \delta = B$; for the ordered-LNO $A_2BB'O_6$, $\beta = \delta = A$, $\gamma = B$, $\alpha = B'$; for the ordered-ilmenite $A_2BB'O_6$, $\beta = \gamma = A$, $\delta = B$, $\alpha = B'$. At left, ξ_1 (or ξ_2) is the distance between β (or δ) and the oxygen plane that it penetrates during the polarization reversal.

the ordered-LNO $A_2BB'O_6$ is $AB - AB'-$, and the ordered-ilmenite $A_2BB'O_6$ is $AB - B'A-$. Other combinations, such as $AA - BB-$, are connected to the four existing types as explained in Sec. II B.

B. Coherent FE polarization reversal

Experimentally, the FE polarization reversal process is a complicated one that typically proceeds by nucleation and motion of domain walls, involving both intrinsic atomic motion and extrinsic pinning by defects. In this paper we have chosen to focus only on coherent FE domain reversal, in which every unit cell undergoes the polarization reversal simultaneously. This coherent reversal process is clearly highly oversimplified, but previous studies of perovskite oxides have shown that the coherent barrier provides a figure of merit that is often a useful indicator of the real barrier to polarization reversal. For example, the well-known FE perovskite $PbTiO_3$ has a coherent barrier around 0.2 eV per five-atom cell [10], so perovskite oxides with barriers lower than this may be considered likely to be FE.

The atomic origin of ferroelectricity in LNO is well understood [15,16]. In LNO, the polarization reversal is driven by an infrared-active (IR-active) mode that is associated with the motion of Li cations along the rhombohedral axis. In the reversal process, each Li cation penetrates through an oxygen plane and migrates into an adjacent unoccupied oxygen octahedron. In our notation, the polarization reversal process interchanges Li with $-$, so that the polar structure changes from $LiNb - LiNb-$ to its inversion image $-NbLi-NbLi$.

For all types of polar corundum derivatives, we assume that the polarization reversal mechanism is similar to that of LNO, i.e., that the reversal process interchanges A or B with $-$. The structures before and after this process are listed in Table I. Under such an operation, the LNO-type structure is transformed into its own inversion-reversed image, which is a typical FE behavior. The same is true for the ordered-LNO structure. By contrast, the ilmenite-type $AB - BA-$ is transformed into $BB - AA-$, and the ordered-ilmenite $AB - B'A-$ into $BB' - AA-$. These structures are not inversion equivalent to the starting structures. Moreover, they exhibit face-sharing A-containing octahedra, making them relatively unfavorable energetically. Additionally, both the ilmenite structure and its switched partner are centrosymmetric. For these reasons, we exclude the ilmenite and ordered-ilmenite structures from further consideration as FE candidates.

TABLE I. Corundum-derived structures before and after polarization reversal.

	Before	After
LNO-type	$AB-AB-$	$-BA-BA$
Ilmenite	$AB-BA-$	$-BB-AA$
Ordered-LNO	$AB-AB'-$	$-BA-B'A$
Ordered ilmenite	$AB-B'A-$	$-BB'-AA$

C. Energy profile calculations

For the LNO-type and the ordered-LNO FE candidates, we firstly analyze the symmetry of the reversal path. The ground state symmetry is R3c for the LNO-type materials, and R3 for the ordered-LNO ones, but the symmetry of the reversal path is not straightforward. In this paper, we assume that the threefold rotation is always preserved, so that the symmetry of the path can only be R3c or R3 for the LNO-type case, and R3 for the ordered-LNO case. If the structure acquires an inversion center at the midpoint of the path when the polarization is zero ($R\bar{3}c$ or $R\bar{3}$ for the two cases, respectively), the energy profile would be symmetric. If the inversion symmetry at the midpoint is broken, as for example by magnetic ordering, the energy profile would be asymmetric.

Based on the symmetry of the reversal path, we adopt different methods to calculate the energy profile of the FE reversal. In the case when the inversion symmetry is present at the midpoint structure, the polarization reversal can be analyzed in terms of an unstable IR-active phonon mode at the high-symmetry midpoint. In general, even if the midpoint is not in a high-symmetry reference structure, the motion of the small A cations is responsible for the polarization reversal. As illustrated in Fig. 1, we define ξ_1 (ξ_2) to be the distance between the first (second) A cation and the oxygen plane that it penetrates as this A cation moves along its path. Then $\xi_1 + \xi_2$ is adopted as a "reaction coordinate" to describe the reversal. Finally, we use either the unstable IR-active mode at the midpoint (for the high-symmetry case) or $\xi_1 + \xi_2$ (otherwise) as a structural constraint, and relax all other internal structural degrees of freedom while stepping through a sequence of values of this constraint. This gives us the energy profile along the path, from which the energy barrier is obtained by inspection.

D. First-principles methods

Our calculations are performed with plane-wave density functional theory (DFT) implemented in VASP [34]. The exchange-correlation functional that we use is PBEsol, a revised Perdew-Burke-Ernzerhof generalized-gradient approximation that improves equilibrium properties of densely-packed solids [35]. The ionic core environment is simulated by projector augmented-wave (PAW) pseudopotentials [36]. For transition metal elements Mn and Fe, we use a Hubbard $U = 4.2$ eV on the $3d$ orbitals [28,37]. For the Os $5d$ orbital, we use a Hubbard $U = 1.4$ eV [31]. The magnetic moments are collinear and spin-orbit coupling is neglected. The cutoff energy for all calculations is 550 eV. The energy error threshold varied slightly in different calculations, but an accuracy between 1.0×10^{-5} and 1.0×10^{-7} eV is achieved in all calculations. The forces are reduced below 0.001 eV/Angstrom for calculations of structural relaxation. A $6\times6\times6$ Monkhorst-Pack k-mesh is used in the calculations. Linear-response methods are used to calculate the Γ-point force-constant matrices. The spontaneous polarization is calculated using the Berry phase formalism [38].

III. RESULTS AND DISCUSSION

In this paper, we apply the method of calculating the energy profile described in Sec. II C to fully analyze the coherent FE reversal path of the LNO-type corundum derivatives $LiNbO_3$ [14], $LiTaO_3$ [14], $ZnSnO_3$ [20], $FeTiO_3$ [18,19], and $MnTiO_3$ [18] and the ordered-LNO corundum derivatives Li_2ZrTeO_6 [25], Li_2HfTeO_6 [25], Mn_2FeWO_6 [30], Mn_3WO_6 [32], and Zn_2FeOsO_6 [31].

A. Ground state structure and magnetic order

The properties of FE materials are sensitive to atomic displacements and strain, so it is essential to start our calculation with accurate structural parameters. The lattice constants and Wyckoff positions obtained from our calculations are summarized in the Supplemental Material [33], with experimental results provided for reference. Our structural parameters are very close to the experimental results. The oxidation states, obtained by rounding the integrated charge around each cation, are also displayed in Table II and are in good agreement with experimental observations.

The on-site magnetic moments are investigated for $FeTiO_3$, $MnTiO_3$, Mn_2FeWO_6, Mn_3WO_6, and Zn_2FeOsO_6 by integrating the spin density inside the PAW sphere. Our DFT+U calculation predict that the magnetic moment is about 3.7 μ_B on each Fe^{2+}, 4.6 μ_B on each Mn^{2+}, and 4.2 μ_B on Fe^{3+}. These results are in agreement with the d^6 state of Fe^{2+} and the d^5 configuration of Fe^{3+} and Mn^{2+}. The magnetic moment on Os^{5+} is 2.1 μ_B from our calculation, which is consistent with the high-spin d^3 state after taking into account the screening of the Os moment arising from the hybridization between Os $5d$ and O $2p$ orbitals.

The energy of different magnetic orderings is also studied. In our calculation, we only consider magnetic structures that preserve the periodicity of the rhombohedral unit cell. Our results suggest that the ground-state magnetic ordering is antiferromagnetic (AFM) for $FeTiO_3$ and $MnTiO_3$ and ferrimagnetic (FiM) for Zn_2FeOsO_6. To investigate the magnetic structures of Mn_2FeWO_6 and Mn_3WO_6, four different types of unit cell are considered in the calculation. We adopt a notation like "udu" to describe the possible spin structure on the three cations excepting W. Here "u" is spin-up, "d" is spin-down, and the spins are given on cations A_1, A_2, and B in that order, where A_1 and A_2 are face sharing with B' and B cations, respectively. (Note that A_1, A_2 and B correspond to cations β, δ, and γ, respectively, in Fig. 1.) The four possible states (not counting those that are trivially related by a global spin reversal) are uuu, uud, udu, and udd. The energy of each fully-relaxed magnetic structure is listed in the Supplemental Material [33]. Of those, the most stable state for both Mn_2FeWO_6 and Mn_3WO_6 is udu. However, for Mn_3WO_6, the energy difference between the uud and udu states is tiny, so we considered the polarization reversal for both magnetic states.

TABLE II. Oxidation states of the LNO-type ABO_3 and the ordered-LNO $A_2BB'O_6$ corundum derivatives. The oxidation state of O ion is -2 in all materials.

LNO-type	A	B	Ordered LNO	A	B	B'
$LiNbO_3$	+1	+5	Li_2ZrTeO_6	+1	+4	+6
$LiTaO_3$	+1	+5	Li_2HfTeO_6	+1	+4	+6
$ZnSnO_3$	+2	+4	Mn_2FeWO_6	+2	+2	+6
$FeTiO_3$	+2	+4	Mn_3WO_6	+2	+2	+6
$MnTiO_3$	+2	+4	Zn_2FeOsO_6	+2	+3	+5

B. Symmetry of the reversal path

For the LNO-type materials, the simplest possible reversal path would be one in which the two A cations move synchronously, so that $\xi_1 = \xi_2$ everywhere along the path. In this case the symmetry along the path is R3c, except at the midpoint where there is an inversion center and the symmetry becomes R$\bar{3}$c. Another possibility is that the cations move sequentially, one after the other, so that $\xi_1 \neq \xi_2$ for at least part of the path. In this case the symmetry is R3 except at the R$\bar{3}$ midpoint. In order to find out which scenario occurs, we calculate the energy of the midpoint structures with symmetry R$\bar{3}$c and R$\bar{3}$ respectively; the results are shown in Table III.

TABLE III. The energy and the unstable phonon modes at the midpoint structure of $LiNbO_3$, $LiTaO_3$, $ZnSnO_3$, $FeTiO_3$, and $MnTiO_3$ with symmetry R$\bar{3}$c and R$\bar{3}$. The energy of the ground-state structure is set to be zero as reference and the unit is meV per unit cell. The imaginary frequency of the unstable phonon is given in units of cm^{-1}.

	Energy		Unstable modes		
	R$\bar{3}$c	R$\bar{3}$	R$\bar{3}$c		R$\bar{3}$
			A_{2u}	A_{2g}	A_u
$LiNbO_3$	303	259	216i	123i	158i
$LiTaO_3$	163	129	178i	116i	1i
$ZnSnO_3$	255	241	93i	30i	47i
$FeTiO_3$	1014	735	195i	75i	–
$MnTiO_3$	550	468	177i	73i	114i

For all LNO-type materials that we have studied, the $R\bar{3}$ midpoint structure is energetically favored, which implies that the reversal occurs via the lower-symmetry R3→ $R\bar{3}$ →R3 scenario, at least in the central portion of the path. This striking result demonstrates that the midpoint of the FE reversal path in the LNO-type FE materials is *not* identified with the high-temperature paraelectric structure [15,16] but instead has lower symmetry.

The energy differences between $R\bar{3}c$ and $R\bar{3}$ structures can be explained by comparing their unstable phonons, for which the frequencies are listed in Table III. At $R\bar{3}c$ symmetry, all the LNO-type candidates have *two* unstable modes along the rhombohedral axis direction, namely one A_{2u} and one A_{2g} mode. The A_{2u} mode is IR active, and it describes the synchronous movement of A cations. The nonpolar A_{2g} mode, however, is related to the out-of-phase movement of the two A cations. Comparing the unstable modes in the $R\bar{3}c$ and $R\bar{3}$ structures, we find that the unstable nonpolar mode is absent in the $R\bar{3}$ structure. Therefore, the unstable A_{2g} mode is responsible for the energy reduction in going from the $R\bar{3}c$ to the $R\bar{3}$ structure. In addition, we find an unstable E_u mode in $LiNbO_3$ and $FeTiO_3$ for both the $R\bar{3}c$ and $R\bar{3}$ structures. As the threefold rotational symmetry is preserved in our calculation, the E_u modes are not allowed to relax and further lower the energy.

For the ordered-LNO materials, since the two A cations are not related by any symmetry even in the ground state, the two A cations move sequentially so that $\xi_1 \neq \xi_2$. Therefore, the reversal path adopts the R3 symmetry, except at the $R\bar{3}$ midpoint. The only exception in our calculations is the case of the *udu* magnetic state in Mn_2FeWO_6 and Mn_3WO_6, where the magnetic moments break inversion symmetry so that the midpoint structure slightly deviates from $R\bar{3}$ to R3. Leaving aside this small distortion, the midpoint structures of the LNO-type and the ordered-LNO paths have the same structural symmetry, even though the ordered-LNO compounds have lower symmetry in their ground state.

The sequence of movements of the A cations along the FE reversal path is illustrated in Fig. 2, and described quantitatively using our computed results for $LiNbO_3$ and Mn_2FeWO_6 as paradigmatic examples in Fig. 3. The "Before" and "After" structures in Fig. 2 correspond to the points at the top right and bottom left corners of Fig. 3, respectively. For the LNO-type case, the ideal $R\bar{3}c$ "Midpoint" structure would correspond to the origin on the plot, but the reversal path does not pass through this point because of an unstable A_{2g} mode along the $\xi_1 = -\xi_2$ direction. The "bubble" in the center confirms the significant effect of the unstable A_{2g} mode. Our "Midpoint" in Fig. 2 is thus displaced from the origin along the line $\xi_1 = -\xi_2$. There is a spontaneous breaking of symmetry at the point where the structure departs from the $\xi_1 = \xi_2$ diagonal; at this point the system "randomly" makes a choice between two equivalent paths, marked by filled and open red symbols in Fig. 3.

For the ordered-LNO materials the two A cations are inequivalent, and one of them is already closer to the oxygen plane in the ground state. Let this be the one labeled by ξ_1. It is energetically favorable for this particular A cation to migrate first in the reversal path, which causes either the B or B' cation to be sandwiched between two A cations in the

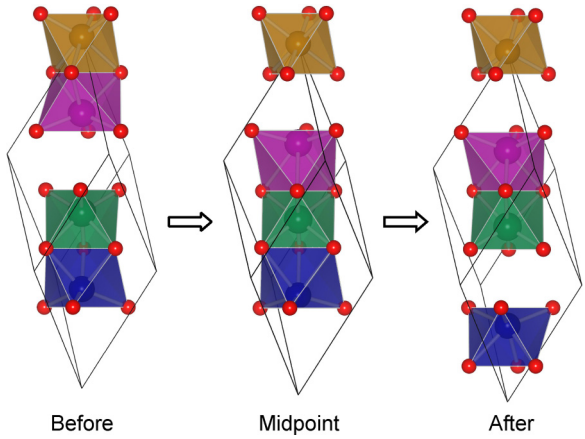

FIG. 2. Structural evolution along the polarization reversal path of the LNO-type and the ordered-LNO corundum derivatives. "Before" and "After" are the initial and final structures on the reversal path with symmetry R3c for the LNO-type and R3 for the ordered-LNO corundum derivatives; "Midpoint" denotes the structure halfway between these and exhibits $R\bar{3}$ structural symmetry in both cases.

"Midpoint" structure as illustrated in Fig. 2. The system thus deterministically follows the path indicated by the full blue line in Fig. 3, with the configuration always staying on one side of the $\xi_1 = \xi_2$ diagonal. If we would reverse the convention on

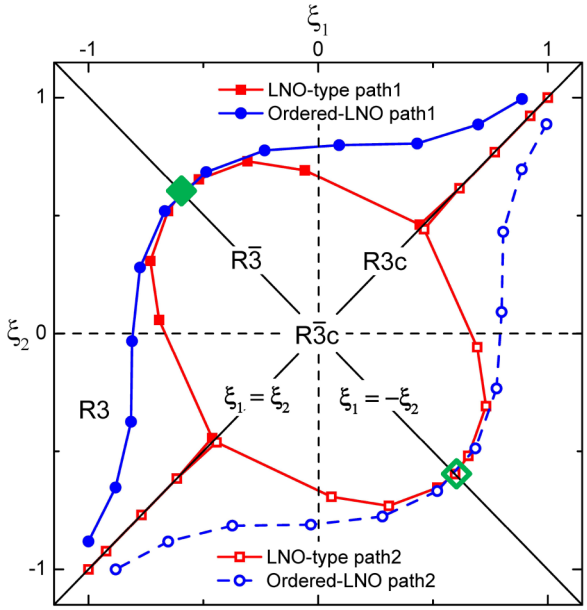

FIG. 3. Movements of A cations in LNO-type (red, here $LiNbO_3$) and ordered-LNO (blue, here Mn_2FeWO_6) corundum derivatives along the polarization reversal path. ξ_1 and ξ_2 are the distances from A atoms to the oxygen planes that are penetrated during the polarization reversal, here rescaled to a range between −1 and 1. The symmetry at an arbitrary (ξ_1,ξ_2) point is R3; on the $\xi_1 = \xi_2$ and $\xi_1 = -\xi_2$ diagonals it is raised to R3c and $R\bar{3}$, respectively; and at the origin ($\xi_1 = \xi_2 = 0$) it reaches $R\bar{3}c$. Green diamonds denote the midpoint structure in the parameter space. In the LNO-type case "path1" and "path2" (filled and open red square symbols) are equivalent and equally probable, while the ordered-LNO system deterministically follows "path1" (full blue line), which becomes "path2" (dashed blue) under a relabeling $\xi_1 \leftrightarrow \xi_2$.

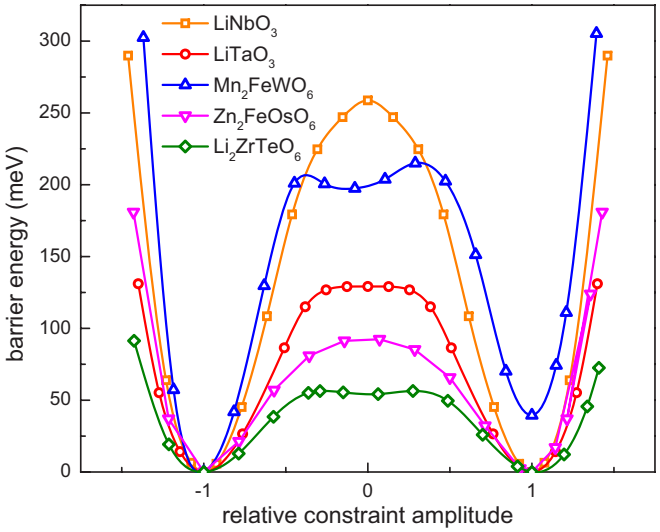

FIG. 4. The polarization reversal energy profile for $LiNbO_3$, $LiTaO_3$, Mn_2FeWO_6, Zn_2FeOsO_6, and Li_2ZrTeO_6.

the definition of ξ_1 and ξ_2, the system would be described by the dashed blue path in Fig. 3.

C. Polarization reversal barrier

Using the methods described in Secs. II C and II D, we compute the relaxed structures and energies for a sequence of constrained values of our "reaction coordinate" $\xi = \xi_1 + \xi_2$ for each material of interest. A selection of results for the energy along the path are presented in Fig. 4, and quantitative results for the energy barrier E_{barrier} and the spontaneous polarization P_S in the ground-state structure are reported in Table IV. For Mn_3WO_6 and Mn_2FeWO_6 with *udu* magnetic ordering, the FE reversal changes the magnetic state to *duu*, so that the energy profile is no longer symmetric and the two minima become inequivalent. For these two compounds, the value of the energy barrier in Table IV is that of the highest barrier along the transformation path.

We find that the cations that are sandwiched in the midpoint structures of ordered-LNO candidates are Zr for Li_2ZrTeO_6, Hf for Li_2HfTeO_6, W for Mn_2FeWO_6 and Mn_3WO_6, and Os for Zn_2FeOsO_6. These results are consistent with the analysis of ξ_1 and ξ_2 in the ground state, as mentioned in Sec. III B. We find that the energy difference between the B and B' sandwiched midpoint structures can be attributed mainly to the Madelung

TABLE IV. Coherent polarization reversal barrier E_{barrier} (meV) per unit cell and spontaneous polarization P_S ($\mu C/cm^2$) for FE candidates.

LNO-type	E_{barrier}	P_S	Ordered-LNO	E_{barrier}	P_S
$LiNbO_3$	259	82	Li_2ZrTeO_6	57	33
$LiTaO_3$	129	57	Li_2HfTeO_6	61	32
$ZnSnO_3$	241	57	Mn_2FeWO_6	215	63
$FeTiO_3$	763	105	*uud* Mn_3WO_6	240	69
$MnTiO_3$	468	94	*udu* Mn_3WO_6	272	70
			Zn_2FeOsO_6	92	52

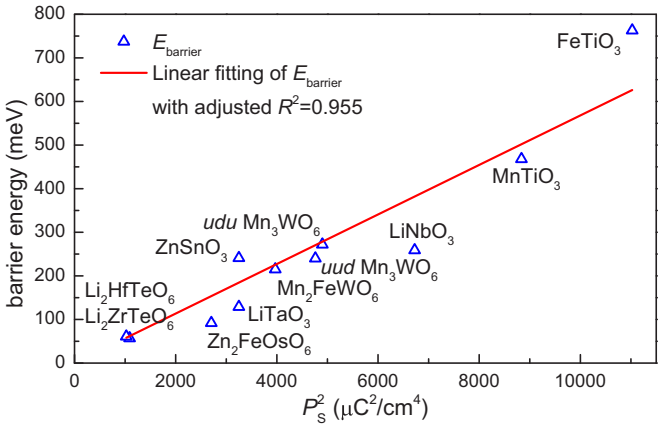

FIG. 5. Empirical proportionality between the coherent FE energy barrier and P_S^2. The red curve is the fitting polynomial $E_{\text{barrier}} = (\mu/2)P_S^2$, with $\mu/2 = 0.057$ meV $cm^4/\mu C^2$.

energy, as shown in the Supplemental Material [33]. Among the computed energy barriers, those for $ZnSnO_3$, Li_2ZrTeO_6, Li_2HfTeO_6, Mn_2FeWO_6, Mn_3WO_6, and Zn_2FeOsO_6 are lower than or comparable to those of the established FE materials $LiNbO_3$ and $LiTaO_3$.

We have analyzed our calculations in an attempt to extract empirical rules of thumb that may help point in the direction of more new materials with low reversal barriers. Firstly, we have considered how the energy barriers are correlated with the spontaneous polarizations. In a FE material the energy E is often approximated as a double well of the form $E(P) = E_0 - \mu P^2 + \nu P^4$ with positive μ and ν. Minimizing $E(P)$ within this model gives the spontaneous polarization as $P_S^2 = \mu/2\nu$ and the energy barrier $E_{\text{barrier}} = E(0) - E(P_S) = \mu^2/4\nu$, which can also be written as $E_{\text{barrier}} = (\mu/2)P_S^2$. Thus, as long as μ can be taken as approximately constant, E_{barrier} is proportional to P_S^2. Interestingly, we find that our computed coherent barrier energies E_{barrier} roughly follow this trend with $\mu/2 = 0.057$ meV $cm^4/\mu C^2$ as shown in Fig. 5. Therefore we suggest that FE corundum derivatives are more likely to be discovered in materials having a relatively low spontaneous polarization.

Furthermore, we have investigated the correlation between the spontaneous polarizations and the geometric properties of the crystals. Our results suggest that for each FE candidate, the polarization P along the reversal path is almost linearly related to the reaction coordinate ξ. Expecting $P(\xi)$ to be an odd function, we add a small cubic part and fit it as $P(\xi) = m\xi + n\xi^3$. The parameters m and n are different in each material, and they are determined by several factors that are not included in the reaction coordinate ξ, such as the displacements of the B cations and the valence states of the A cations. Despite these differences between materials, we find that the spontaneous polarizations P_S of corundum derivatives are correlated with the reaction coordinate ξ_S in the spontaneously polarized ground state, as shown in Fig. 6. This time a roughly linear fit will clearly not work. Again we try fitting $P_S(\xi_S)$ to an odd third-order polynomial and find that $P_S = m\xi_S + n\xi_S^3$ gives a reasonable fit with $m = 13.3\times10^8 \mu C/cm^3$ and $n = 19.0\times10^{24} \mu C/cm^5$ as shown in

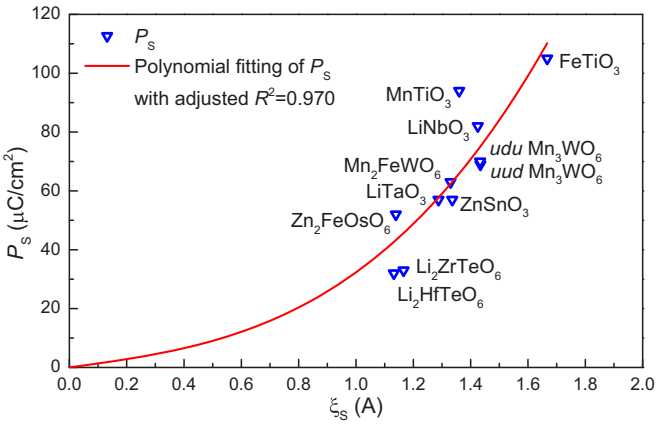

FIG. 6. Empirical correlation between the spontaneous polarization and the reaction coordinate ξ in the ground state. The red curve is the fitting polynomial $P_S = m\xi_S + n\xi_S^3$ with $m = 13.3\times10^8\mu\text{C/cm}^3$ and $n = 19.0\times10^{24}\mu\text{C/cm}^5$.

the figure. As the distance between A cations and oxygen planes can be experimentally determined, this empirical rule can provide a rough estimation of the spontaneous polarization.

D. Insulating vs conducting

Our density-of-states calculations (not shown) indicate that $FeTiO_3$ and Mn_2FeWO_6 become conducting for cation configurations close to the central portion of the reversal path. A detailed analysis of the occupied d orbitals along the path reveals the reason for this metal-insulator transition. In the local octahedral environment of the ground state, the d orbitals are split into triply degenerated t_{2g} and doubly degenerated e_g orbitals. Under the threefold rotational symmetry, the t_{2g} orbitals are further split into a_{1g} and doubly degenerate e'_g irreps. The a_{1g} state has orbital character d_{z^2} with charge lobes directed along the rhombohedral axis, and since these lie closer to the neighboring cations, the energy of the a_{1g} state is lowered. Therefore, the ground-state arrangement of d orbitals in order of increasing energy is a_{1g} followed by e'_g and then e_g. In $FeTiO_3$ and Mn_2FeWO_6, Fe is in the 2+ valence state and has a d^6 configuration. In the ground state, five electrons fully occupy one spin channel and the remaining one occupies the a_{1g} orbital in the minority spin channel. However, during the polarization reversal process, the Fe^{2+} ion temporarily moves away from its neighboring cations, and as a result, the a_{1g} orbital is no longer energetically favored. Instead, the minority electron occupies the doubly degenerate e'_g orbitals, leading to a metallic state. Since a metallic state along the polarization reversal path could short out the applied bias, it may be that the switching of polarization is not possible in such cases. We propose that d^3, d^5, and d^8 orbital configurations should be much more likely to avoid this conducting problem, and are therefore more suitable targets in the search for ferroelectrically switchable magnetic corundum derivatives.

IV. SUMMARY

In this paper, we have proposed a method to study the coherent FE reversal path of the corundum derivative family. By analyzing the structures, we have shown that only the LNO-type and the ordered-LNO corundum derivatives can be FE in the usual sense. We have calculated the energy profiles of the reversal paths using first-principles density-functional methods. Our calculations reveal that the symmetry of the FE barrier structure is lower than that of the paraelectric phase. According to our calculations, $ZnSnO_3$, Li_2ZrTeO_6, Li_2HfTeO_6, Mn_3WO_6, and Zn_2FeOsO_6 are predicted to be possible new FE materials. We have found empirically that the energy barrier is roughly proportional to the the square of the spontaneous polarization, and that the spontaneous polarization is strongly correlated with the reaction coordinate ξ in the ground state. Finally, we have also argued that magnetic corundum derivatives are unlikely to be suitable for FE switching unless the magnetic ion is d^3, d^5, or d^8, since metallic configurations otherwise tend to appear along the FE reversal path.

ACKNOWLEDGMENT

We thank Martha Greenblatt and Manrong Li for many useful discussions. The work was supported by Office of Naval Research Grant No. N00014-12-1-1035.

[1] K. M. Rabe, H. Ahn Charles, and Jean-Marc Triscone, *Physics of Ferroelectrics* (Springer-Verlag, Berlin Heidelberg, 2008).
[2] J. F. Scott, *Ferroelectric Memories* (Springer-Verlag, Berlin Heidelberg, 2000).
[3] W. Eerenstein, N. D. Mathur, and J. F. Scott, Nature (London) **442**, 759 (2006).
[4] S.-W. Cheong and M. Mostovoy, Nat. Mater. **6**, 13 (2007).
[5] R. Ramesh and N. A. Spaldin, Nat. Mater. **6**, 21 (2007).
[6] K. F. Wang, J.-M. Liu, and Z. F. Ren, Adv. Phys. **58**, 321 (2009).
[7] D. Khomskii, Physics **2**, 20 (2009).
[8] P. Barone and S. Picozzi, C. R. Phys. **16**, 143 (2015).
[9] J. Varignon, N. C. Bristowe, É. Bousquet, and P. Ghosez, C. R. Phys. **16**, 153 (2015).
[10] R. E. Cohen, Nature (London) **358**, 136 (1992).
[11] D. Vanderbilt, Curr. Opin. Solid State Mater. Sci. **2**, 701 (1997).
[12] A. T. Mulder, N. A. Benedek, J. M. Rondinelli, and C. J. Fennie, Adv. Funct. Mater. **23**, 4810 (2013).
[13] H. J. Zhao, W. Ren, Y. Yang, J. Íñiguez, X. M. Chen, and L. Bellaiche, Nat. Commun. **5**, 4021 (2014).
[14] A. M. Glass and M. E. Lines, Phys. Rev. B **13**, 180 (1976).
[15] I. Inbar and R. E. Cohen, Phys. Rev. B **53**, 1193 (1996).
[16] M. Veithen and Ph. Ghosez, Phys. Rev. B **65**, 214302 (2002).
[17] A. W. Sleight and C. T. Prewitt, Mater. Res. Bull. **5**, 207 (1970).
[18] C. J. Fennie, Phys. Rev. Lett. **100**, 167203 (2008).
[19] T. Varga, A. Kumar, E. Vlahos, S. Denev, M. Park, S. Hong, T. Sanehira, Y. Wang, C. J. Fennie, S. K. Streiffer, X. Ke, P. Schiffer, V. Gopalan, and J. F. Mitchell, Phys. Rev. Lett. **103**, 047601 (2009).
[20] J. Y. Son, G. Lee, M.-H. Jo, H. Kim, H. M. Jang, and Y.-H. Shin, J. Am. Chem. Soc. **131**, 8386 (2009).

[21] Y. Inaguma, M. Yoshida, T. Tsuchiya, A. Aimi, K. Tanaka, T. Katsumata, and D. Mori, J. Phys.: Conf. Ser. **215**, 012131 (2010).

[22] A. Aimi, T. Katsumata, D. Mori, D. Fu, M. Itoh, T. Kyômen, K. Hiraki, T. Takahashi, and Y. Inaguma, Inorg. Chem. **50**, 6392 (2011)

[23] X. F. Hao, A. Stroppa, S. Picozzi, A. Filippetti, and C. Franchini, Phys. Rev. B **86**, 014116 (2012).

[24] T. Kawamoto, K. Fujita, I. Yamada, T. Matoba, S. J. Kim, P. Gao, X. Pan, S. D. Findlay, C. Tassel, H. Kageyama, A. J. Studer, J. Hester, T. Irifune, H. Akamatsu, and K. Tanaka, J. Am. Chem. Soc. **136**, 15291 (2014).

[25] J. Choisnet, A. Rulmont, and P. Tarte, J. Solid State Chem. **75**, 124 (1988).

[26] R. Mathieu, S. A. Ivanov, G. V. Bazuev, M. Hudl, P. Lazor, I. V. Solovyev, and P. Nordblad, Appl. Phys. Lett. **98**, 202505 (2011).

[27] M.-R. Li, D. Walker, M. Retuerto, T. Sarkar, J. Hadermann, P. W. Stephens, M. Croft, A. Ignatov, C. P. Grams, J. Hemberger, I. Nowik, P. S. Halasyamani, T. T. Tran, S. Mukherjee, T. S. Dasgupta, and M. Greenblatt, Angew. Chem. Int. Ed. **52**, 8406 (2013).

[28] M.-R. Li, M. Retuerto, D. Walker, T. Sarkar, P. W. Stephens, S. Mukherjee, T. S. Dasgupta, J. P. Hodges, M. Croft, C. P. Grams, J. Hemberger, J. Sánchez-Benítez, A. Huq, F. O. Saouma, J. I. Jang, and M. Greenblatt, Angew. Chem. Int. Ed. **53**, 10774 (2014).

[29] M.-R. Li, P. W. Stephens, M. Retuerto, T. Sarkar, C. P. Grams, J. Hemberger, M. C. Croft, D. Walker, and M. Greenblatt, J. Am. Chem. Soc. **136**, 8508 (2014).

[30] M.-R. Li, M. Croft, P. W. Stephens, M. Ye, D. Vanderbilt, M. Retuerto, Z. Deng, C. P. Grams, J. Hemberger, J. Hadermann, W.-M. Li, C.-Q. Jin, F. O. Saouma, J. I. Jang, H. Akamatsu, V. Gopalan, D. Walker, and M. Greenblatt, Adv. Mater. **27**, 2177 (2015).

[31] P. S. Wang, W. Ren, L. Bellaiche, and H. J. Xiang, Phys. Rev. Lett. **114**, 147204 (2015).

[32] Private communication with Prof. Martha Greenblatt and Dr. Manrong Li.

[33] See Supplemental Material at http://link.aps.org/supplemental/10.1103/PhysRevB.93.134303 for information of the lattice constants, Wyckoff positions, energy of different magnetic orderings, and energy of different midpoint structures covered by this study.

[34] G. Kresse and J. Furthmüller, Phys. Rev. B **54**, 11169 (1996).

[35] J. P. Perdew, A. Ruzsinszky, G. I. Csonka, O. A. Vydrov, G. E. Scuseria, L. A. Constantin, X. Zhou, and K. Burke, Phys. Rev. Lett. **100**, 136406 (2008).

[36] P. E. Blochl, Phys. Rev. B **50**, 17953 (1994); G. Kresse and D. Joubert, *ibid.* **59**, 1758 (1999).

[37] S. L. Dudarev, G. A. Botton, S. Y. Savrasov, C. J. Humphreys, and A. P. Sutton, Phys. Rev. B **57**, 1505 (1998).

[38] R. D. King-Smith and D. Vanderbilt, Phys. Rev. B **47**, 1651 (1993).

Supplement: Ferroelectricity in corundum derivatives

Meng Ye[1,*] and David Vanderbilt[1]

[1] *Department of Physics & Astronomy, Rutgers University, Piscataway, New Jersey 08854, USA*

(Dated: March 22, 2016)

The properties of FE materials are sensitive to atomic displacements and strain, so it is essential to start our calculation with accurate structural parameters. The lattice constants and Wyckoff positions obtained from our calculations are summarized in the Tables I and II, with experimental results provided for reference. Our structure parameters are very close to the experimental results.

To investigate the magnetic structures of Mn_2FeWO_6 and Mn_3WO_6, four different types of unit cell are considered in the calculation. We adopt a notation like "*udu*" to describe the possible spin structure, where "*u*" is spin-up, "*d*" is spin-down, and the spins are given on atom β, δ and γ, in that order. The four possible states (not counting those that are trivially related by a global spin reversal) are *uuu*, *uud*, *udu*, and *udd*. The energy of each fully-relaxed magnetic structure is listed in Table III. Of those, the most stable state for both Mn_2FeWO_6 and Mn_3WO_6 is *udu*. However, for Mn_3WO_6, the energy difference between the *uud* and *udu* states is tiny, so we considered the polarization reversal for both magnetic states.

The magnetic ground states of Mn_2FeWO_6 and Mn_3WO_6 can be understood by analyzing the super-exchange interactions between A_1, A_2 and B cations (also shown as β, γ and δ cations). The magnetic moments are coupled through the oxygen octahedra, and there are three independent coupling constants. The moments on A_2 and B sites are coupled through face-sharing and corner-sharing oxygen octahedra with strength J_{A_2B}; the A_1 and B moments are coupled through edge-sharing octahedra with strength J_{A_1B}; and the A_1 and A_2 moments are coupled through corner-sharing octahedra with strength $J_{A_1A_2}$. Then the magnetic energy $E_{\rm mag}$ can be written as

$$E_{\rm mag} = J_{A_1B}\hat{S}_{A_1}\cdot\hat{S}_B + J_{A_2B}\hat{S}_{A_2}\cdot\hat{S}_B + J_{A_1A_2}\hat{S}_{A_1}\cdot\hat{S}_{A_2}\,, \tag{1}$$

where $\hat{S}$ represent the spin on each site. Substituting the energy of different magnetic orderings in Table III into Eq.(1), we find that the coupling constants are all positive. This result implies that the three magnetic moments all favor AFM coupling. However, it is impossible to make three collinear spins couple antiferromagnetically, and this frustration implies that one pair must be ferromagnetically coupled.

In Table IV we list the relative spin orientations of the magnetic ions. Since the face-sharing coupling J_{A_2B} is the strongest, it is not surprising that the A_2 and B moments couple antiferromagnetically; the competition between J_{A_1B} and $J_{A_1A_2}$ then determines the magnetic ground state. In Mn_3WO_6, these two couplings are comparable, so the energy difference between the *uud* and *udu* states is tiny. In the case of Mn_2FeWO_6, the magnetic moment on the B cation is smaller, so the coupling J_{A_1B} is weaker than $J_{A_1A_2}$. Therefore, the lowest-energy state is *udu*.

For the ordered-LNO materials the two A cations are inequivalent, and one of them is already closer to the oxygen plane in the ground state ($\xi_{1S} \neq \xi_{2S}$). Therefore it is energetically favorable for this particular A cation to migrate first in the reversal path, which causes either the B or B' cation to be sandwiched between two A cations in the midpoint structure. If $\xi_{1S} > \xi_{2S}$, the sandwiched cation is B; otherwise it is B'. By calculating the energy difference $\Delta E = E_B - E_{B'}$ between the B and B' sandwiched midpoint structures, we find that the cations that are sandwiched in the midpoint structures are Zr for Li_2ZrTeO_6, Hf for Li_2HfTeO_6, W for Mn_2FeWO_6 and Mn_3WO_6, and Os for Zn_2FeOsO_6. These results are consistent with the analysis of ξ_{1S} and ξ_{2S}, as shown in Table V. We find that the energy difference between the two distinct midpoint structures is mainly due to the difference $\Delta E^{\rm M} = E^{\rm M}_B - E^{\rm M}_{B'}$ between the Madelung energies of the two structures in a simple point-ion model, as shown in Table. V.

---

* Electronic address: mengye@physics.rutgers.edu

[1] S. C. Abrahams, W. C. Hamilton, J. M. Reddy, J. Phys. Chem. Solids **27**, 1013 (1966).
[2] M. Ohgaki, K. Tanaka, F. Marumo, Mineralogical Journal (Japan) **14**, 373 (1989).
[3] Y. Inaguma, M. Yoshida, T. Katsumata, J. Am. Chem. Soc. **130**, 6704 (2008).
[4] K. Leinenweber, J. Linton, A. Navrotsky, Y. Fei, J.B. Parise, Phys. Chem. Miner. **22**, 251 (1995).
[5] A. M. Arévalo-López and J. P. Attfield, Phys. Rev. B **88**, 104416 (2013).
[6] J. Choisnet, A. Rulmont, P.Tarte, J. Solid State Chem. **75**, 124 (1988).
[7] M.-R. Li, M. Croft, P. W. Stephens, M. Ye, D. Vanderbilt, M. Retuerto, Z. Deng, C. P. Grams, J. Hemberger, J. Hadermann, W.-M. Li, C.-Q. Jin, F. O. Saouma, J. I. Jang, H. Akamatsu, V. Gopalan, D. Walker, and M. Greenblatt, Adv. Mater. **27**, 2177 (2015).
[8] Private communication with Prof. Martha Greenblatt and Dr. Manrong Li.

TABLE I: Rhombohedral structural parameters of LNO-type ABO_3 corundum derivatives $LiNbO_3$, $LiTaO_3$, $ZnSnO_3$, $FeTiO_3$ and $MnTiO_3$ from first-principles calculations and experiments. The Wyckoff positions are 2a for A and B cations, and 6c for oxygen anions (note that $A_x = A_y = A_z$ and $B_x = B_y = B_z$). The origin is defined by setting the Wyckoff position B_x to zero.

		Lattice constants		Wyckoff positions				
		a (Å)	α (°)	A_x	B_x	O_x	O_y	O_z
$LiNbO_3$	Calc.	5.486	56.0	0.282	0.000	0.360	0.719	0.112
	Exp.[1]	5.494	55.9	0.280	0.000	0.359	0.720	0.111
$LiTaO_3$	Calc.	5.476	56.2	0.284	0.000	0.365	0.726	0.119
	Exp.[2]	5.473	56.2	0.291	0.000	0.368	0.732	0.124
$ZnSnO_3$	Calc.	5.584	56.5	0.283	0.000	0.392	0.709	0.104
	Exp.[3]	5.569	56.4	0.286	0.000	0.381	0.721	0.111
$FeTiO_3$	Calc.	5.434	56.5	0.290	0.000	0.364	0.721	0.104
	Exp.[4]	5.458	56.0	0.287	0.000	0.364	0.720	0.109
$MnTiO_3$	Calc.	5.481	56.6	0.279	0.000	0.348	0.721	0.120
	Exp.[5]	5.455	56.8	0.276	0.000	0.345	0.731	0.128

TABLE II: Rhombohedral structure parameters of ordered-LNO $A_2BB'O_6$ corundum derivatives Li_2ZrTeO_6, Li_2HfTeO_6, Mn_2FeWO_6, Mn_3WO_6 and Zn_2FeOsO_6 from first-principles calculations and experiments. Wyckoff positions are 1a for A_1, A_2, B and B' cations, and 3b for O_1 and O_2 anions. The origin is defined by setting the Wyckoff position B'_x to zero. For ordered-LNO Mn_3WO_6 and Zn_2FeOsO_6, no experimental results are available.

		Magnetic	Lattice constants		Wyckoff position									
		order	a (Å)	α (°)	A_{1x}	A_{2x}	B_x	B'_x	O_{1x}	O_{1y}	O_{1z}	O_{2x}	O_{2y}	O_{2z}
Li_2ZrTeO_6	Calc.	—	5.526	56.1	0.291	0.781	0.504	0.000	0.366	0.745	0.111	0.628	0.219	0.895
	Exp.[6]	—	5.497	56.1	0.298	0.768	0.507	0.000	0.390	0.729	0.133	0.621	0.235	0.893
Li_2HfTeO_6	Calc.	—	5.480	56.3	0.289	0.781	0.504	0.000	0.366	0.743	0.115	0.629	0.222	0.889
	Exp.	—	NA	NA	NA	NA	NA	NA	NA	NA	NA	NA	NA	NA
Mn_2FeWO_6	Calc.	*udu*	5.531	57.3	0.286	0.787	0.506	0.000	0.356	0.744	0.109	0.632	0.207	0.884
	Exp.[7]	NA	5.562	56.9	0.278	0.785	0.493	0.000	0.347	0.745	0.102	0.631	0.197	0.885
Mn_3WO_6	Calc.	*udu*	5.607	56.7	0.287	0.790	0.508	0.000	0.356	0.742	0.102	0.631	0.199	0.893
	Calc.	*uud*	5.613	56.6	0.283	0.779	0.493	0.000	0.384	0.693	0.124	0.595	0.234	0.848
	Exp.[8]	NA	5.605	56.7	0.283	0.788	0.510	0.000	0.351	0.744	0.104	0.631	0.190	0.901
Zn_2FeOsO_6	Calc.	FiM	5.410	56.7	0.284	0.783	0.504	0.000	0.376	0.732	0.114	0.619	0.223	0.885
	Exp.	NA	NA	NA	NA	NA	NA	NA	NA	NA	NA	NA	NA	NA

TABLE III: Magnetic energy of different magnetic states relative to the lowest-energy state in Mn_2FeWO_6 and Mn_3WO_6, in units of meV per formula unit (f.u.).

	Energy (meV/f.u.)			
	uuu	*uud*	*udd*	*udu*
Mn_2FeWO_6	90.2	32.1	39.5	0.0
Mn_3WO_6	101.8	1.0	19.2	0.0

TABLE IV: Relative spin direction between different magnetic ions in Mn_2FeWO_6 and Mn_3WO_6.

	uuu	*uud*	*udd*	*udu*
A_1 and B	FM	AFM	FM	AFM
A_2 and B	FM	AFM	AFM	FM
A_1 and A_2	FM	FM	AFM	AFM

TABLE V: Ground state and midpoint structures of ordered-LNO candidates and the energy differences between B and B' sandwiched midpoint structures. The distances between A cations and the oxygen planes in the ground state are characterized by ξ_{1S} and ξ_{2S}. The energy difference between the B and B' sandwiched midpoint structures is ΔE. The Madelung energy difference between the B and B' sandwiched midpoint structures is ΔE^{M}.

Ordered-LNO	B	B'	Sandwiched cation	ξ_{1S} (Å)	ξ_{2S} (Å)	ΔE^{M} (meV)	ΔE (meV)
Li_2ZrTeO_6	Zr	Te	Zr	0.607	0.559	−186	−48
Li_2HfTeO_6	Hf	Te	Hf	0.582	0.550	−94	−29
Mn_2FeWO_6	Fe	W	W	0.623	0.707	2085	225
uud Mn_3WO_6	Mn	W	W	0.635	0.799	1666	266
udu Mn_3WO_6	Mn	W	W	0.642	0.790	1499	290
Zn_2FeOsO_6	Fe	Os	Os	0.565	0.574	382	102